

Title	Fabrication of ultra-dense sub-10 nm in-plane Si nanowire arrays by using a novel block copolymer method: optical properties
Authors	Ghoshal, Tandra;Ntaras, Christos;O'Connell, John;Shaw, Matthew T.;Holmes, Justin D.;Avgeropoulos, Apostolos;Morris, Michael A.
Publication date	2015-12-22
Original Citation	Ghoshal, T., Ntaras, C., O'Connell, J., Shaw, M. T., Holmes, J. D., Avgeropoulos, A. and Morris, M. A. (2016) 'Fabrication of ultra-dense sub-10 nm in-plane Si nanowire arrays by using a novel block copolymer method: optical properties', Nanoscale, 8(4), pp. 2177-2187. doi: 10.1039/C5NR07085F
Type of publication	Article (peer-reviewed)
Link to publisher's version	<a href="http://pubs.rsc.org/en/content/articlepdf/2016/nr/c5nr07085f - 10.1039/C5NR07085F">http://pubs.rsc.org/en/content/articlepdf/2016/nr/c5nr07085f - 10.1039/C5NR07085F</a>
Rights	© The Royal Society of Chemistry 2016
Download date	2023-05-04 21:24:25
Item downloaded from	<a href="http://hdl.handle.net/10468/6741">http://hdl.handle.net/10468/6741</a>



# UCC

**University College Cork, Ireland**  
 Coláiste na hOllscoile Corcaigh

# **Fabrication of ultra-dense sub-10 nm in-plane Si nanowire arrays from a novel block copolymer method: optical properties**

Tandra Ghoshal,<sup>\*1,2</sup> Christos Ntaras,<sup>3</sup> John O'Connell,<sup>1</sup> Matthew T. Shaw,<sup>4</sup> Justin D. Holmes,<sup>1,2</sup> Apostolos Avgeropoulos,<sup>3</sup> Michael A. Morris<sup>\*1,2</sup>

<sup>1</sup>Materials research group, Department of Chemistry and Tyndall National Institute, University College Cork, Cork, Ireland

<sup>2</sup>AMBER (Advanced Materials and Biological Engineering Research Centre), Trinity College Dublin, Dublin, Ireland

<sup>3</sup>Department of Materials Science Engineering, University of Ioannina, Ioannina, Greece

<sup>4</sup>Intel Ireland Ltd., Collinstown Industrial Estate, Co. Kildare, Ireland

[\*] Corresponding Author: Prof. Michael A. Morris

Tel: + 353 21 490 2180

Fax: +353 21 427 4097

E-mail: m.morris@ucc.ie

and Dr. Tandra Ghoshal

Tel: + 353 21 490 2911

Fax: +353 21 427 4097

E-mail: g\_tandra@yahoo.co.in

In an effort we have used low- $\chi$ , symmetric block copolymer as an alternative to the high- $\chi$  systems currently being translated towards industrial silicon chip manufacture. Here, methodology for generating on-chip, etch resistant etch masks and subsequent pattern transfer to substrate using ultra-small dimension, lamellar, microphase separated polystyrene-b-poly(ethylene oxide) (PS-b-PEO) block copolymer (BCP) is described. Well-controlled films of a perpendicularly oriented lamellar pattern with a feature size of  $\sim 8$  nm were achieved through amplification of the effective interaction parameter ( $\chi_{\text{eff}}$ ) of the BCP system. The self-assembled films were used as ‘templates’ for the generation of inorganic oxides nanowire arrays through selective metal ion inclusion and subsequent processing. Inclusion is a significant challenge because the lamellar systems have less chemical and mechanical robustness than the cylinder forming materials. The oxide nanowires were isolated of uniform diameter ( $\sim 8$  nm) and their structure mimics the original BCP nanopatterns. We demonstrate that these lamellar phase iron oxide nanowire arrays could be used as resist mask to fabricate densely packed, identical ordered, good fidelity silicon nanowire arrays on the substrate. Possible applications of the materials prepared are discussed, in particular, in the area of photonics and the photoluminescence where the properties are found to be similar to those of surface-oxidized silicon nanocrystals and porous silicon.

## Introduction

The continual reduction of critical dimensions (CDs) of advanced semiconductor devices has necessitated the development of expensive multiple patterning techniques in ultraviolet (UV) lithography.<sup>1</sup> The directed self-assembly (DSA) of block copolymers (BCPs) is being explored as a cost-effective, robust and scalable method for next generation hole<sup>2</sup> and line/space patterns<sup>3</sup>. BCP self assembly (microphase separation) can provide a means of dense sub-10 nm scale nanopatterns over large substrate areas and these patterns can be used as masks, templates or scaffolds for the fabrication of nanostructured materials arrays for application such as high density transistor circuitry, storage media, photovoltaics and sensors<sup>4-8</sup>. A number of different morphologies are possible dependent on (i) the chemical incompatibility of the blocks (indicated by the Flory-Huggins interaction parameter,  $\chi$ ), (ii) molecular weight, (iii) degree of polymerization  $N$  and (iv) the block volume fraction.<sup>8-12</sup> For line-space patterning, symmetric lamellar-forming BCP systems that exhibit domain orientation perpendicular are of particular interest since their pattern transfer to a substrate is conceptually simple and various structures or components of integrated circuits (ICs) such as contacts, interconnects, gates for the current planar as well as future 3D devices might be fabricated.<sup>13</sup> The successful integration of BCP methods into silicon device industrial fabrication not only requires ultimate control of the self-assembly but also the pattern transfer process.<sup>14</sup> However, etching becomes complicated when feature size reduce and etch limitations of BCP patterns can lead to silicon features of low aspect ratio and high line edge roughness (LER). To overcome this barrier, a 'hard mask' material with extremely high selectivity could be used.<sup>15-16</sup>

Lamellar forming polystyrene-*b*-polymethylmethacrylate (PS-*b*-PMMA) has been the pre-eminent system of interest because of its availability, ease of synthesis, and well-developed processing strategies.<sup>2, 17-18</sup> Despite considerable progress, there are challenges such as long

processing times<sup>19</sup>, the requirement of careful interface engineering to define domain orientation<sup>20</sup> and minimum feature size being above expected roadmap targets<sup>21</sup>. The polystyrene-b-polyethylene oxide (PS-b-PEO) system is a highly attractive alternative material capable of extension to sub 10 nm feature size. Asymmetric PS-b-PEO systems are well studied and exhibit high degrees of lateral ordering with short processing times without any substrate surface modification.<sup>22-26</sup> Importantly, this has considerable additional functionality because the chemistry of PEO allows for insertion of metal species and formation of inorganic patterns for various lithographic and biological applications<sup>15-16, 27-28</sup>. However, symmetric PS-b-PEO has hardly been studied. Applications of PS-b-PEO lamellar forming systems in nanolithography have yet to be demonstrated despite ease of pattern transfer and propensity to form line-space structures.

To address the paucity of work and provide a methodology towards achieving very low feature size silicon nanostructures we have studied a symmetric, lamellar forming PS-b-PEO. Extending established methodology from cylinder to lamellar compositions was not facile and required significant method evolution. The transitions from a 3D morphology to 2D introduce mechanical and chemical frailty which requires new inclusion procedures and solvents. The insitu metal ion inclusion technique<sup>16, 22-23, 29</sup> previously reported for the hexagonal phase PS-PEO system, was therefore customized to fabricate inorganic oxide hard mask lamellar nanopatterns which allowed high fidelity pattern transfer into silicon so as to produce high aspect ratio, highly ordered periodic Si line patterns.

## Experimental Section

### Materials

The polymer PS-b-PEO with molecular weight 10800 kg mol<sup>-1</sup> was synthesized (See Supporting Information). The solvents toluene, anhydrous alcohol (ETH), 2-propanol and Lithium chloride (LiCl) were purchased from Sigma Aldrich. Single crystal (100) boron

doped (P type) silicon wafers with a native silica layer were used as the experimental substrates. For filtration, Fluoropore™ PTFE filter membranes with the pore size 0.2  $\mu\text{m}$ , diameter of 25 mm was used.

### **Procedure for microphase separation and inorganic oxide pattern formation**

Substrates were cleaned by ultrasonication in acetone and toluene (30 min each) and dried under nitrogen. 5 ml. of 1 wt% PS-*b*-PEO solution in toluene was stirred for 12 h at room temperature. LiCl was dissolved in ethanol and in THF separately to make 2.5 g L<sup>-1</sup> solution. Then the necessary amount of LiCl/ethanol or LiCl/THF solution (varying from 0.025 ml to 2 ml) was added to the prepared PS-*b*-PEO/toluene solution with a micropipette. The solution was stirred for different times between 15 min to 2 h for salt complexation to take place. The resultant solution was filtered and spin coated immediately onto the substrate at 3000 rpm for 30 s. The films were exposed to toluene vapour in a closed vessel kept at 50°C for 30 min to induce microphase separation. After solvent annealing for the desired time, the films were dried under nitrogen. For the fabrication of iron oxide and nickel oxide nanowires, Iron (III) nitrate nonahydrate ( $\text{Fe}(\text{NO}_3)_3 \cdot 9\text{H}_2\text{O}$ ) and nickel nitrate hexahydrate ( $\text{Ni}(\text{NO}_3)_2 \cdot 6\text{H}_2\text{O}$ ) were dissolved in ethanol/2-propanol and spin-coated directly onto the microphase separated film. UV/Ozone treatment was used to oxidize the precursor and remove polymer. The concentrations of the iron precursor, the solution stirring time etc. were varied to optimize inclusion. The thermal stability of the nanowires was verified by annealing them at 800°C for 1 h.

### **Pattern transfer using ICP etch**

These iron oxide nanowire arrays were used as a hard mask for pattern transfer to the substrate using an STS, Advanced Oxide Etch (AOE) ICP etcher as previously reported.<sup>15, 29</sup> The system has two different RF generators, one, to generate and control the plasma density by direct connection to the antenna coil, while the other one was used to adjust and control

the energy of the ions by connecting it to the substrate holder. During etching, the sample was thermally bonded to a cooled chuck (10<sup>0</sup>C) with a pressure 9.5 Torr. For Si nanowire fabrication, the process used a controlled gas mixture of C<sub>4</sub>F<sub>8</sub>/SF<sub>6</sub> at flow rates of 90 sccm/30 sccm respectively and the ICP and RIE power were set to 600 W and 15 W respectively at a chamber pressure of 15 mTorr. The etch time was varied to vary the depth of the wires.

### **Characterizations**

Surface morphologies were imaged by scanning probe microscopy (SPM, Park systems, XE-100) in tapping mode and Helium ion scanning electron microscopy (Carl Zeiss HIM). The film thicknesses were measured by optical ellipsometer (Woolam M2000) and electron microscopy (i.e. cross-sections). Sample cross-sections were prepared for the Transmission electron microscopy (TEM) imaging using an FEI Helios Nanolab 600i system containing a high resolution Elstar™ Schottky field-emission SEM and a Sidewinder FIB column. These were then imaged by a JEOL 2100 and TEM, FEI Titan instrument. Fourier Transform Infrared Spectrometry (FTIR) spectra were recorded on infrared spectrometer (IR 660, Varian). X-Ray photoelectron spectroscopy (XPS) experiments were conducted on a Thermo K-alpha machine with Al K<sub>α</sub> X-ray source operating at 72 W. The photoluminescence measurements were carried out at room temperature with a Fluorescence spectrophotometer (Perkin-Elmer LS 50 B). Raman spectra were recorded using a SPEX 1403 monochromator equipped with a dc detection device. The 488 nm laser line of an Ar ion laser was used for excitation with an output power of 20 mW.

### **Results and Discussion**

Polymer synthesis and pattern formation have been extensively discussed elsewhere and are only summarized here.<sup>30</sup> The polymer characterization results for this lamellar phase system of molecular weights of PS = 5.5 and PEO = 5.3 kg mol<sup>-1</sup> are reported in our previous work (see Supporting Information). Thermo-solvent annealing was used to achieve thin films of

ordered, microphase separated, perpendicularly oriented lamellae structures. In the absence of the lithium ions, no ordered structures could be formed. The morphology of the PS-b-PEO thin film with the addition of 0.05 ml of LiCl-THF following solvent annealing in toluene at 60° C for 30 min are shown in Fig. 1. Solvent annealing results in the formation of perpendicularly oriented ordered arrangement of alternating PS and PEO lamellae (PEO is darker in colour in the AFM image). In Scheme 1, (A) and (B) represents the spin coated and solvent annealed perpendicularly oriented lamellar BCP film respectively. The films exhibit longer line-like morphology across the substrate area with an average lamellar domain spacing (L) of 15 nm from both the AFM and SEM images and this value (+/- 2%) was observed for all films. The ellipsometry measured thickness (d) of the film is ~ 22 nm. Note that no surface treatment or modifications with random copolymer brushes is necessary to ordain the vertical domain orientation. The internal morphology and interface of the film with the substrate surface is further analysed using TEM of FIB thinned cross-sections. Generally, the similarity of the PS ( $1.05 \text{ g cm}^{-3}$ ) and amorphous PEO ( $1.12 \text{ g cm}^{-3}$ ) densities results in featureless TEM micrographs<sup>16</sup> and this was observed here. However, the PEO selective inclusion of  $\text{Li}^+$  ions enhances the electron contrast. Inset of Fig. 1a shows the cross-sectional TEM image of the periodic ordered lamellar film prepared with the addition of LiCl-THF after solvent annealing in toluene at 60° C for 30 min. The image did not reveal the lamellar structure but instead periodic dark spots of varying diameter of 2-6 nm in the centre of the film were resolved. The data suggest that solvent annealing does not result in PEO crystallization even at a temperature higher than its melting point since the crystalline form has higher density ( $1.24 \text{ g cm}^{-3}$ )<sup>31</sup> and might be expected to provide TEM contrast.<sup>32</sup> This is further described in detail elsewhere.<sup>30</sup> The polymer film shows no indication of deformation or delamination at the substrate interface and the TEM derived thickness of 22 nm is consistent with ellipsometry measurement.



In this report, a low molecular weight PS-b-PEO BCP was shown to form well-ordered lamellar structures despite a sub-optimum value of  $\chi N = 7.71$ . However, the segregation strength ( $\chi N$ ) has been increased by the addition of Li ions in micromolar or millimolar concentrations.<sup>33</sup> This enhancement of the  $\chi_{\text{eff}}$  has been achieved by the formation of lithium-PEO complexes which increases the order-disorder transition temperature ( $T_{\text{ODT}}$ ).<sup>34-35</sup> It has been proposed that the oxygen atoms belonging to the PEO chain coordinate the cations and localized in the middle of the PEO lamellae in the form of pseudo ionic micelles due to nonuniform local stresses in the lamellae and the coupling between  $\text{Li}^+$  coordination and these stresses as evidenced by TEM cross-sections.<sup>36-37</sup> These coordinated lithium ions creates a separation of charge (cation-anion) which leads to periodically ordered self-assembled structures on the surface. It can instantly be seen that the vertical orientation maximizes the distance of the lithium centres from the interfaces and maximizes the distance between these centres and so lowers the energy of the system considerably. We suggest that this is a possible explanation for this vertical lamellae alignment across the substrate.<sup>30</sup>

For a symmetric BCP system, careful manipulation of the surface/interfacial energies is needed to achieve the monolayer of perpendicular orientation of the lamellae which depends on the interplay between the film thickness and the natural period.<sup>38-40</sup> For the PS-b-PEO system, the blocks exhibit asymmetric affinities for the solid substrate and the air interface where the hydrophilic PEO will preferentially wet the substrate surface (favourable PEO-substrate interactions) whilst PS will tend to segregate to a vacuum interface to form a PS-rich layer (PS has a lower surface energy,  $\gamma_{\text{PS}} = 33 \text{ mNm}^{-1}$ ;  $\gamma_{\text{PEO}} = 43 \text{ mNm}^{-1}$ ).<sup>22</sup> The film thickness was varied (changing the polymer concentrations) from 0.5 L to 2 L in order to understand the self-assembly process, the orientation of the lamellae and the structural variation (See Supporting Information). No ordering is achieved for the film thickness below L. When the film thickness was increased to just above L ( $\sim 17 \text{ nm}$ ), localized ordering with

short stripes and plateau without any ordering coexist. For the thickness of  $\sim 1.5L$  (22 nm), long continuous stripes where lamellae oriented perpendicular to the substrate are realized over the substrate area. Although local area defects in the form of small particulate or absence of patterns (below 25 nm<sup>2</sup> area) are observed, no large area dewetting or thickness undulation is evident. Further thickness increment ( $> 22$  nm) results the coexistence of parallel (island) and perpendicular lamellae orientation. Longer continuous line-like patterns with perpendicular lamellar arrangements over 2-4  $\mu\text{m}$  area were formed with increasing film thickness to 30 nm. But the film thickness used in this study is  $\sim 22$  nm to achieve a monolayer of the lamellae for the simplicity and ease in the fabrication of Si nanowires through the pattern transfer process. Note that the addition of Li ions at the centre of the film also contributes towards the thickness of the film.

The fabrication of inorganic oxides nanowire arrays using the BCP lamellar nanopatterns as a template is illustrated in Scheme 1. No activation/modification of the PEO lamellae is required for generating the oxide arrays as was previously needed for the hexagonal phase BCP systems.<sup>16, 22-23, 29</sup> Well-ordered oxide nanowire arrays can be created by the metal ion inclusion method through directly spin coating the precursor-2 propanol solution and subsequent UV/Ozone treatment demonstrated by (C) and (D) in Scheme 1. After metal ion inclusion, UV/ozone treatment was carried out immediately so as to remove any solvent, oxidize and cross-link metal ions forming oxide and remove the organic part simultaneously. It might be noted that a brief UV/Ozone treatment to cross-link the metal ions followed by air calcinations can also be pursued for oxidation and complete removal of the residual polymer. Note, however, that direct calcination in the absence of the UV/ozone treatment causes disorder and agglomeration of the nanowires suggesting that the UV/ozone cross-linking process is critical in providing the periodic structure. Fig. 2 shows the AFM and SEM images of well ordered iron (Figs. 2a and b) and nickel oxide (Figs. 2c and d) nanowire arrays

formed after UV/Ozone treatment. The nanowires had uniform size/shape and their placement mimics the original self-assembled block copolymer patterns. The average diameters of the nanowires were 8 nm with a spacing of 14-16 nm. The concentrations of the precursor solutions were tuned to form uniform, continuous and smooth nanowire patterns. The average nanowire heights were between 4-6 nm as measured by ellipsometry. Note that the optimum metal ion solution concentrations differ when alternative metal precursors were used suggesting the rate of cation uptake is species sensitive. The nanowires were well adhered to the substrate and thermally robust (See Supporting Information). Diameter and thickness variation along the nanowires is visible in few places and this is more prominent for the nickel oxide.

In our previous work for the hexagonal phase system,<sup>16, 22-23, 29</sup> anhydrous alcohol was used to dissolve the metal precursors. Here, 2-propanol was used instead of anhydrous alcohol to reduce the undulation and pattern degradation along the nanowires. This is because of its' vapour pressure, selected solubility into PEO (since they have similar solubility parameters) and chemistry. Ethanol molecules might also have a deleterious impact because of their ability to change the PEO blocks.<sup>23, 29</sup> The hydrophobic nature of PS limits metal ion inclusion into the PS lamellae whilst selective inclusion into the BCP template is favoured by the affinity of PEO with the ionic solution. The spin coating procedure is highly efficient and it is suggested that PEO accelerates the metal ion inclusion process probably via either intra- or intermolecular coordination via electron donation from the PEO block to oxygen species in the 2-propanol molecule.<sup>22</sup> Also, the wetting rate of one material on another is directly dependent on the dissolution kinetics which is related to the reactions occurring between them.<sup>41</sup> The gain in the free energy comes from the high reaction efficiency between PEO and metal cations are considered to create an additional driving force for the inclusion. These data and other materials (TiO<sub>2</sub>, CuO, etc.) made in the laboratories show that this is a facile and

generic means to generate size monodisperse, lamellar nanowires at a substrate surface. Following our previous work,<sup>15</sup> where it was reported that iron oxide nanodots can be an excellent resistant mask for high aspect ratio silicon substrate patterning. Attempts were made to adopt this strategy to produce silicon nanowire arrays by use of the iron oxide wires as a hard mask.

As briefly mentioned above, for the lamellar phase we have determined the optimum amount of iron precursor (1.8 wt%) to generate well defined iron oxide nanowire patterns which show wire uniformity, regular separation and without any pattern degradation. At this optimum concentration, the iron oxide nanowires are continuous; wire-interruption is negligible compared to the wafer area. Figs. 3a-f shows the surface morphology and topography of the films for different precursor concentration with the precursor-2 propanol solution stirred for 30 min. The AFM (a, c, e) and SEM (b, d, f) images displays the patterns for the iron precursor concentrations of 1.5 wt%, 2 wt% and 2.2 wt% respectively. At lower concentration, monolayer, discontinuous line-like patterns were formed though continuous nanowire pattern is visible in few places as evident from both AFM (Fig. 3a) and SEM images (Fig. 3b). With increasing the precursor concentration to 2 wt% (Fig. 3c and d) the nanowires are predominantly continuous but there is enhanced surface roughness, thickness variations (as indicated by bright regions in the AFM image) and pattern degradation (pattern missing) also observed. A closer view in the SEM image (Fig. 3d) reveals that the nanowires were connected by their sidewalls forming a nanoporous structure. No large scale surface roughness or thickness undulation across the surface was noticed. With increasing the concentration to 2.2 wt% (Figs. 3e and f), large scale pattern degradation was noticed. The images are consistent with limited solubility or metal precursor uptake by the PEO lamellae and excess material at the surface results in the disordered morphology. Further increasing the concentrations, a few nanowires are seen in discrete areas but irregular, disconnected and

agglomerated nanowire assemblies with secondary overlayers are dominant (See Supporting Information). Thus, the optimum concentrations range of the precursor-2-propanol is determined between 1.7 to 1.9 wt % and this process is reproducible to achieve continuous iron oxide nanowire patterns.

The optimum precursor-2 propanol solution stirring time for the highest quality desired monolayer lamellar periodic nanowire arrays pattern was determined. Generally, 1.8 wt% precursor concentrations with 30 min stirring time followed by filtration is required for the formation of regular nanowire arrays (Figs. 2a and b). The AFM and SEM images in Figures 4a-f displays the surface morphology and topography of the films for longer precursor solution stirring times to 45, 60 and 90 min respectively. Well resolved periodic ordered nanowire arrays are formed all over the substrate surface but a few nanoparticle type features are also observed indicative of inorganic materials after 45 min stirring time (Figs. 4a-b). Variation in the film thickness and nanowire diameter along their length is also evident. No large area defects are seen. The film maintains the long range ordered lamellar nanowire structures but the defect frequency (in the form of these discrete linear regions or particulates) increased with stirring time (1 h). With increasing the stirring time for 1 h 30 min (Figs. 4e and f), localized nanoparticles or agglomerated 3D nanostructures in the range of 20-200 nm is observed throughout the film surface with structural degradation in several places. No trace of precipitation observed with the stirring time but it is suggested that the inorganic small particulates form because the solution is hygroscopic during stirring. During spin coating and subsequent solvent evaporation, precipitation can occur and the inorganic moieties are oxidized after UV/Ozone treatment.

Note, here, that the filtration of the coating solution is required. The larger ( $> 200$  nm) particles were removed by filtration while small particles remains within the precursor solution. With increased aging time these become aggregated and increased in size (van der

Wals forces). Eventually these become large enough with stirring time to hinder formation of ordered arrangements. In this way, filtration is a critical component of this process if optimum, ordered arrangements are to form.

In few parts of the films has defects such as thickness undulation or small particles on the surface which increases with the precursor concentrations or solution stirring time. This is generally due to spin coating which involves convection of a coating liquid, driven by centrifugal force and evaporation of the solvent simultaneously.<sup>42</sup> After spin coating at room temperature, some residual solvent droplets always remain on the film surface because of surface tension effects and also due to the slower evaporation rate of 2-propanol (some amount of water present). When the precursor solution concentration is low or the solution aged for smaller time, the metal ions diffused and interacted with the PEO implying the absence of any metal ions within the droplets on the surface just after spin coating. But, with increasing the precursor concentrations to a certain extent or with increasing the stirring time, there are unreacted metal ions present within the droplet which oxidized upon exposure to the UV/ozone. An excessive metal precursor concentration might result in oxide depositions all over the substrate (See Supporting Information). This overloading of material is consistent with the proposed preferential PEO solution inclusion model since if this was a simple template mechanism, it would be expected that these non-specific surface depositions would be seen throughout the solution concentration range.<sup>43</sup>

The precursor solvent/s plays an important role in achieving periodic oxide nanowire arrays with low-defect densities. Films prepared with a precursor-2 propanol combination (Figs. 2a and b) exhibits smoother surfaces of uniform thickness across the substrate area compared to the precursor-ethanol (Figs. 5a and b) systems. Well resolved large area periodic oxide nanowire arrays were formed but micro-defects in the form of small particulate (diameter 25-250 nm) without any patterns are observed all over the substrate area for the

precursor-ethanol system. Further, nanowires of varying diameter along their length are also seen.

Above, the microphase separated PS-b-PEO structure was prepared using a LiCl-THF solution. The choice of solvent was critical. LiCl-ethanol solutions can also be used but THF solutions are advantageous. The microphase separated films prepared with LiCl-THF exhibit a smoother polymer surface of uniform thickness across the substrate area compared to the LiCl-ethanol systems. More micro-defects in the form of small particulate (diameter 25-250 nm) or homogeneously distributed dark spots without any patterns are observed for the LiCl-ethanol systems for all the solvent annealed films. The defect density observed is around  $4 \times 10^4/\text{cm}^2$  (calculated from AFM and SEM images) which decreases considerably with reference to both in density ( $\sim 10$  times) and sizes for the LiCl-THF system. Further, fingerprint pattern with smaller consistent length lamellar morphology is noticed for the LiCl-ethanol system.<sup>30</sup> Faster hydrolyzation rate is realized by dissolving the salt in ethanol than that of THF, form small particulates of LiOH in solution due to more hygroscopic nature of anhydrous alcohol than THF. Alcohol rapidly absorbs water from atmosphere, further hydrolyze the Li salt (LiCl is hygroscopic) which hinders the phase segregation process and creates defects all over the substrate area. These films were also used as a template to fabricate iron oxide nanowire arrays using similar inclusion method. The as-prepared iron oxide nanowires follow similar self-assembled BCP line patterns (Figs. 5c and d). The nanowires have uniform diameter throughout their entire length for the optimum precursor concentrations used. Thickness undulation or small diameter variation also observed in few places. This suggests that the inclusion technique is the direct result of solubility of metal precursor within the PEO.

The internal morphology and interface of the iron oxide nanowire arrays with the substrate surface was further analysed using TEM cross-sections. The adhesion of the materials is

reflected in the mechanical integrity (i.e. no interfacial cracks etc. at the interface of the wires with the substrate) of the structures during FIB processing. We suggest this approach offers advantages over lithographic patterning of a oxide film where interfacial tensions can result in delamination and mechanical damage under strain.<sup>44</sup> The cross-sectional TEM image shows well-separated equidistant nanowires supported on the passive silica substrate surface (Fig. 6a). The average diameters and height of the nanowires were 8 nm and 4 nm respectively with a lamellar spacing of 15 nm (as previously seen by AFM and SEM detailed above). Elemental composition was confirmed by high resolution EDAX mapping and the distribution of Fe, O and Si are shown in Fig. 6b. The Fe map shows a homogeneous distribution of Fe corresponding to each nanowire and a sharp elemental interface to the substrate surface suggesting no inter-diffusion occurs. The O and Si maps confirm the presence of oxides on the nanowire and passive layer and the substrate.

The chemical composition of the iron oxide nanowires before (UV/Ozone alone) and after annealing was confirmed by Fe 2p XPS studies. Prior to annealing, the Fe 2p core level spectrum of the as-formed iron oxide nanowires (Fig. 6c) consists of peaks at 711.1 eV (Fe 2p<sub>3/2</sub>) and 724.5 eV (Fe 2p<sub>1/2</sub>) which are broadened due to the presence of Fe<sup>+2</sup> and Fe<sup>+3</sup> ions. Curve-fitting using Gaussian-Lorentzian line shapes provides individual binding energies of 709.6/722.9 eV (assigned to Fe<sup>+2</sup>) and 711.5/724.9 eV (Fe<sup>+3</sup>) in agreement with literature assignments.<sup>45</sup> The Fe<sup>+3</sup>/ Fe<sup>+2</sup> ratio was estimated to about 2:1 as expected for Fe<sub>3</sub>O<sub>4</sub>. Following calcination the Fe 2p core level spectrum (See Supporting Information) consists of two sharp peaks at 711.4/725.2 eV corresponding to the Fe 2p<sub>3/2</sub> and Fe 2p<sub>1/2</sub> signals. A high binding energy satellite (+8 eV shift) can also be seen and these data are consistent with formation of Fe<sub>2</sub>O<sub>3</sub>.<sup>46-47</sup> A typical XPS survey spectrum (See Supporting Information) of iron oxide nanowires after annealing confirms the expected presence of Si, O, C and Fe. The C1s feature is relatively small and demonstrates effective removal of carbon species during



UV/Ozone treatment. Its' intensity is consistent with adventitious material formed by adsorption and other contamination during sample preparation. Similar nature was observed from Ni 2p spectra for nickel oxide which confirms both  $\text{Ni}^{+2}$  and  $\text{Ni}^{+3}$  in nickel (III) oxide (after UV/Ozone treatment) transformed to NiO, nickel (II) oxide after annealing (See Supporting Information).<sup>48</sup>

Fig. 6d shows FTIR absorption spectra of the iron oxide nanowire arrays formed after UV/Ozone treatment and further annealing. A band centred at  $678\text{ cm}^{-1}$  can be assigned to neutral charged oxygen vacancies possibly nonbridging oxygen hole centres (NBOHCs) or similar compounds in  $\beta$ -cristobalite, a silica polymorph.<sup>49</sup> The feature at  $1070\text{ cm}^{-1}$  is associated with stretching vibration modes of the Si-O-Si bonds in  $\text{SiO}_2$ .<sup>50</sup> The shape and intensity of these peaks are almost similar for both the samples. An additional strong peak at  $630\text{ cm}^{-1}$  and  $540\text{ cm}^{-1}$  is observed for the iron oxide nanowire arrays formed after UV/Ozone treatment and further annealing respectively. These peaks corresponds to the most intense peak of magnetite ( $\text{Fe}_3\text{O}_4$ ) and hematite ( $\text{Fe}_2\text{O}_3$ ) respectively.<sup>51</sup>

In order to fabricate Si nanowire arrays on the substrate surface, the iron oxide nanowires were used as a hard mask in the ICP etch process. For the pattern transfer, the iron oxide nanowires were prepared by using the optimum precursor concentrations (1.8 wt% iron nitrate-2-propanol). A mild oxalic acid aqueous solution was used to remove undesired  $\text{Fe}_3\text{O}_4$  from the as-formed Si nanowire arrays. Fig. 7a shows highly dense, periodic Si nanowire arrays with iron oxide at top over large substrate areas following a 30 sec Si etch. A higher magnification image (inset of Fig. 7a) demonstrate that the nanowires are continuous and of regular diameter (7 nm) along the length with a lamellar spacing of 15 nm. This implies that the etching does not damage the original 'mask' to a significant extent. The depth of the nanowires can be varied by increasing the Si etch time and Figs. 7a-c represents the SEM images of the nanowire arrays following etches of 30 sec, 45 sec and 1 min respectively. All

the images reveal large scale fabrication of ordered continuous high density Si nanowire arrays with smooth sidewalls demonstrating the mask effectiveness. Note that further increases in etch time may results in nanowire discontinuity in few areas (See Supporting Information). It is not clear of this is due to iron oxide etch mask degradation or mechanical weakness of the samples. The iron oxide nanostructures prepared for lower and higher concentrations of precursors also shows significant contrast enhancement with identical pattern after the Si etch (See Supporting Information). Thus, the fabricated Si nanopatterns were solely following the original mask patterns on Si substrate.

Cross-sectional TEM was used to fully characterize the nanowires. Fig. 7d show micrographs of the well ordered lamellar array of 30 sec etched nanowires on Si substrates with iron oxide at top. The images reveal Si nanowires of about 10 nm heights with a 2 nm silica layer and 4 nm iron oxide masks at top. The lamellar spacing remains unchanged. All of the wires investigated had smooth sidewalls as revealed by the higher magnification TEM image. The diameter of the nanowires decreases along its' length towards top of the wire due to etch selectivity between silica and silicon. In our previous works, it was demonstrated that the iron oxide is an excellent resistant mask to fabricate vertically and horizontally aligned Si nanorods and nanowires through consecutive silica and Si etch processes.<sup>15, 23, 29</sup> In this case, only the Si etch recipe is followed to fabricate the Si nanowires which erode the native silica inhomogeneously and further the top portion of the silicon. The nanowires have sharp tips which have potential application for field emission devices. Importantly, the HRTEM image (inset of Fig. 7d) reveals a highly crystalline structure with no sign of etch related amorphization. Note also that the lattice fringes are continuous between bulk and nanowire silicon indicating no stacking or other defects and hence no re-crystallization during etching. The image shows the lattice fringes with spacing  $3.11 \text{ \AA}$  across the wires agrees reasonably well with the Si FCC (111) interplanar distances.<sup>52</sup> The  $54^\circ$  angle of the (111) fringes with the

substrate surface plane is consistent with the (100) orientation of the Si wafer. Also, from both TEM and HRTEM images, it can be confirmed that the diameter and thickness of the iron oxide mask remains almost similar after the pattern transfer process which reflects the excellence of its masking ability. Thus, highly dense uniform 1D silicon nanowire arrays with controlled crystallographic orientation could be created through selective etching of the silicon wafers of chosen orientations.

Elemental composition was confirmed by high resolution EDAX mapping and the distribution of Fe, O and Si are shown in Figs. 7e. The Si and Fe map shows a homogeneous distribution of silicon corresponding to each nanowire with sharp elemental interface with iron oxide suggesting no inter-diffusion occurs after pattern transfer. The O map confirms the presence of oxides in iron oxide at top and native silica layer of the substrate.

The check the crystallinity of the Si nanowires on Si substrate was further examined by Raman spectroscopy. For the measurement, the samples were immersed in oxalic acid solution (to remove the iron oxide layer on top of the nanowires) and dried.<sup>15</sup> The Raman spectrum obtained is nearly Lorentzian in shape and an intense peak is observed at  $520\text{ cm}^{-1}$  assigned to the first order transverse optical phonon mode of crystalline silicon (Fig. 8a). This peak observed is in the centre of the Brillouin zone due to the conservation of quasi-momentum in crystals. The absence of a secondary peak in Raman spectra confirms that the nanowires retain the crystallinity of bulk silicon wafer. No peak related to the Si nanowire was observed as it was fabricated onto the Si wafer.

Photoluminescence (PL) measurements were performed on the ordered arrays of Si nanowires on the Si substrate in ambient air. Inset of Fig. 8a shows the TEM cross-section of the Si nanowires after removal of iron oxide. Note that the nanowires are not damaged during the oxide removal process and their original profiles and arrangement are unchanged. The PL band is intense with a Gaussian-like characteristics centred at 680 nm ( $\sim 1.82\text{ eV}$ ) under a 325

nm excitation wavelength (Fig. 8b). The same PL spectral region has been reported in literature for different Si/SiO<sub>2</sub> based structures.<sup>53-56</sup> This band position is typical for non-bridging oxygen hole centres (NBOHC) in bulk silica.<sup>57</sup> Note that the NBOHC model of light emitters has also been suggested to explain visible PL from porous silicon<sup>58</sup> and Qin et al.<sup>59-60</sup> explained the visible emission from native oxide on Si wafers which originates from luminescent centres exist in the silica skins of nano-Si particles. It is, therefore, suggested that the PL band from the Si nanowire arrays is associated with the native oxide exist at the top/sidewall of the wires. Further, it is suggested that the luminescent centres originate from the oxygen deficient defects in the Si-SiO<sub>2</sub> interface region.

To confirm the origin of the PL band, the samples were annealed at different temperatures in the range of 200-500<sup>0</sup> C. The PL spectra (Fig. 8b) of all the samples are almost similar, no apparent band shift was observed. An increment in the band intensity was noticed with increasing the annealing temperature. At lower temperatures, the surface oxidation initialized when Si=O bonds or Si-O-Si bonds are formed on the surface of the Si nanowires. At temperatures 400 and 500<sup>0</sup> C, the PL bands become more intense due to an increase in the thickness of the oxide layer on top of the nanowires. When crystalline Si nanowires are oxidized, the Si-Si bonds are likely to weaken because of large stress at the distortion surface. Then the Si-O-Si bonds are more likely to be formed and stabilized the interface, since it requires neither large deformation energy nor an excess element. The oxidation leads to the formation of the localized trap states within the energy bands which originates the intense PL band.

## Conclusion

In summary, we present a simple and cost effective large scale fabrication of high density, horizontal, uniform, lamellar Si nanowire arrays with precise placement on substrate based on insitu hard mask microphase separated BCP approach. Microphase separated well-ordered

perpendicularly oriented lamellae for a symmetric PS-*b*-PEO system with a domain spacing of ~16 nm is achieved by a simple solvent annealing process. A selective metal ion inclusion method followed by UV/Ozone treatment was applied for the generation of oxide nanowire arrays using the self assembled BCP as a template. No surface treatment or modification was applied for the inclusion based on chemical coordination between metal ion and PEO lamellae. This methodology demonstrates a general method for creating sub-10 nm large scale, uniform diameter and smooth sidewall, horizontal high density oxide nanowire arrays. The nanowires are structurally arranged in a mimic of the original self-assembled BCP pattern and show strong adherence to the substrate to high temperature. Large area, identical ordered, crystalline, horizontal Si nanowire (diameter ~ 7 nm) arrays is fabricated with a smooth sidewall profile by using these iron oxide nanowires as a hard mask over silicon. The nanowires observed were crystalline with desirable uni-axial crystallographic orientation. NBOHC was suggested as the source of light emission from the Si nanowire arrays similar to that seen for porous silicon. These sharp tip, highly dense nanowire arrays can be employed to fabricate field emission devices. This self-assembled hardmask nanolithography can also be an important component in the manufacturing of nanoscale devices with high throughput and low cost.

### **Supporting Information**

Supporting Information is available from the RSC publication website.

### **Notes**

The authors declare no competing financial interest.

### **Acknowledgements**

We acknowledge financial support from the Science Foundation Ireland AMBER grant 12/RC/2278 and Semiconductor Research Corporation (SRC) grant 2013-OJ-2444. The

contribution of the Foundation's Principal Investigator support is also acknowledged. We would also like to thank Dr. Patrick Carolan and Dr. Clive Downing for the TEM assistance.

## References and notes

- 1 Emerging Research Devices. In *The International Technology Roadmap for Semiconductors*, 2011; pp 1.
- 2 R. Ruiz, H. M. Kang, F. A. Detcheverry, E. Dobisz, D. S. Kercher, T. R. Albrecht, J. J. de Pablo and P. F. Nealey, *Science* 2008, **321**, 936.
- 3 J. Y. Cheng, D. P. Sanders, H. D. Truong, S. Harrer, A. Friz, S. Holmes, M. Colburn and W. D. Hinsberg, *ACS Nano* 2010, **4**, 4815.
- 4 C. Park, J. Yoon and E. L. Thomas, *Polymer* 2003, **44**, 6725.
- 5 M. X. Fu, Y. F. Zhu, R. Q. Tan and G. Q. Shi, *Adv. Mater.* 2001, **13**, 1874.
- 6 C. R. Martin, *Chem. Mat.* 1996, **8**, 1739.
- 7 M. Seo and M. A. Hillmyer, *Science* 2012, **336**, 1422.
- 8 L. Y. Shi, Y. Zhou, X. H. Fan and Z. H. Shen, *Macromolecules* 2013, **46**, 5308.
- 9 D. Borah, M. Ozmen, S. Rasappa, M. T. Shaw, J. D. Holmes and M. A. Morris, *Langmuir* 2013, **29**, 2809.
- 10 Q. Wang, P. F. Nealey and J. J. de Pablo, *Macromolecules* 2001, **34**, 3458.
- 11 S. Rasappa, D. Borah, C. C. Faulkner, T. Lutz, M. T. Shaw, J. D. Holmes and M. A. Morris, *Nanotechnology* 2013, **24**.
- 12 D. Borah, M. T. Shaw, S. Rasappa, R. A. Farrell, C. O'Mahony, C. M. Faulkner, M. Bosea, P. Gleeson, J. D. Holmes and M. A. Morris, *J. Phys. D-Appl. Phys.* 2011, **44**, 174012.
- 13 J. Xu, S. W. Hong, W. Y. Gu, K. Y. Lee, D. S. Kuo, S. G. Xiao and T. P. Russell, *Adv. Mater.* 2011, **23**, 5755.
- 14 R. A. Farrell, N. T. Kinahan, S. Hansel, K. O. Stuen, N. Petkov, M. T. Shaw, L. E. West, V. Djara, R. J. Dunne, O. G. Varona, P. G. Gleeson, S. J. Jung, H. Y. Kim, M. M. Kolesnik,

T. Lutz, C. P. Murray, J. D. Holmes, P. F. Nealey, G. S. Duesberg, V. Krstic and M. A. Morris, *Nanoscale* 2012, **4**, 3228.

15 T. Ghoshal, R. Senthamaraiannan, M. T. Shaw, J. D. Holmes and M. A. Morris, *Nanoscale* 2012, **4**, 7743.

16 T. Ghoshal, T. Maity, J. F. Godsell, S. Roy and M. A. Morris, *Adv. Mater.* 2012, **24**, 2390.

17 C. M. Bates, T. Seshimo, M. J. Maher, W. J. Durand, J. D. Cushen, L. M. Dean, G. Blachut, C. J. Ellison and C. G. Willson, *Science* 2012, **338**, 775.

18 K. Galatsis, K. L. Wang, M. Ozkan, C. S. Ozkan, Y. Huang, J. P. Chang, H. G. Monbouquette, Y. Chen, P. Nealey and Y. Botros, *Adv. Mater.* 2010, **22**, 769.

19 D. J. C. Herr, *J. Mater. Res.* 2011, **26**, 122.

20 P. Mansky, Y. Liu, E. Huang, T. P. Russell and C. J. Hawker, *Science* 1997, **275**, 1458.

21 Y. Zhao, E. Sivaniah and T. Hashimoto, *Macromolecules* 2008, **41**, 9948.

22 T. Ghoshal, M. T. Shaw, C. T. Bolger, J. D. Holmes and M. A. Morris, *J. Mater. Chem.* 2012, **22**, 12083.

23 T. Ghoshal, T. Maity, R. Senthamaraiannan, M. Shaw, P. Carolan, J. D. Holmes, S. Roy, M. A. Morris, *Scientific Reports* 2013, **3**, 2772.

24 P. Mokarian-Tabari, T. W. Collins, J. D. Holmes and M. A. Morris, *ACS Nano* 2011, **5**, 4617.

25 J. Bang, U. Jeong, D. Y. Ryu, T. P. Russell and C. J. Hawker, *Adv. Mater.* 2009, **21**, 4769.

26 S. H. Kim, M. J. Misner, L. Yang, O. Gang, B. M. Ocko and T. P. Russell, *Macromolecules* 2006, **39**, 8473.

27 S. Kim, S. Lee, J. Ko, J. Son, M. Kim, S. Kang and J. Hong, *Nat. Nanotechnol.* 2012, **7**, 567.

28 C. L. Ren, W. D. Tian, I. Szleifer and Y. Q. Ma, *Macromolecules* 2011, **44**, 1719.

- 29 T. Ghoshal, R. Senthamaraikannan, M. T. Shaw, J. D. Holmes and M. A. Morris, *Adv. Mater.* 2014, **26**, 1207.
- 30 T. Ghoshal, C. Ntaras, M. T. Shaw, J. D. Holmes, A. Avgeropoulos and M. A. Morris, *J. Mater. Chem. C* 2015, **3**, 7216.
- 31 W. Y. Chen, J. X. Zheng, S. Z. D. Cheng, C. Y. Li, P. Huang, L. Zhu, H. M. Xiong, Q. Ge, Y. Guo, R. P. Quirk, B. Lotz, L. F. Deng, C. Wu and E. L. Thomas, *Phys. Rev. Lett.* 2004, **93**, 028301.
- 32 G. H. Michler *Electron Microscopy of Polymers* Springer: 2008.
- 33 L. F. Zhang, K. Yu and A. Eisenberg, *Science* 1996, **272**, 1777.
- 34 T. H. Epps, T. S. Bailey, H. D. Pham and F. S. Bates, *Chem. Mat.* 2002, **14**, 1706.
- 35 T. H. Epps, T. S. Bailey, R. Waletzko and F. S. Bates, *Macromolecules* 2003, **36**, 2873.
- 36 F. F. Xue and S. C. Jiang, *RSC Adv.* 2013, **3**, 23895.
- 37 F. Meyer, J. M. Raquez, P. Verge, I. M. de Arenaza, B. Coto, P. Van Der Voort, E. Meaurio, B. Dervaux, J. R. Sarasua, F. Du Prez and P. Dubois, *Biomacromolecules* 2011, **12**, 4086.
- 38 J. G. Kennemur, L. Yao, F. S. Bates and M. A. Hillmyer, *Macromolecules* 2014, **47**, 1411.
- 39 A. Nunns, J. Gwyther and I. Manners, *Polymer* 2013, **54**, 1269.
- 40 M. Ceresoli, F. F. Lupi, G. Seguíni, K. Sparnacci, V. Gianotti, D. Antonioli, M. Laus, L. Boarino and M. Perego, *Nanotechnology* 2014, **25**.
- 41 P. Muralidhar, E. Bonaccorso, G. K. Auernhammer and H. J. Butt, *Colloid Polym. Sci.* 2011, **289**, 1609.
- 42 S. S. Kucherenko and K. D. Leaver, *J. Micromech. Microeng.* 2000, **10**, 299.
- 43 R. A. Farrell, N. Petkov, M. A. Morris and J. D. Holmes, *J. Colloid Interface Sci.* 2010, **349**, 449.
- 44 C. R. Martin and I. A. Aksay, *J. Electroceram.* 2004, **12**, 53.



- 45 R. Prakash, R. J. Choudhary, L. S. S. Chandra, N. Lakshmi and D. M. Phase, *J. Phys.-Condes. Matter* 2007, **19**.
- 46 P. Mills and J. L. Sullivan, *J. Phys. D-Appl. Phys.* 1983, **16**, 723.
- 47 T. Fujii, F. M. F. de Groot, G. A. Sawatzky, F. C. Voogt, T. Hibma and K. Okada, *Physical Review B* 1999, **59**, 3195.
- 48 A. P. Grosvenor, M. C. Biesinger, R. S. Smart and N. S. McIntyre, *Surf. Sci.* 2006, **600**, 1771.
- 49 T. Morioka, S. Kimura, N. Tsuda, C. Kaito, Y. Saito and C. Koike, *Mon. Not. Roy. Astron. Soc.* 1998, **299**, 78.
- 50 P. G. Pai, S. S. Chao, Y. Takagi and G. Lucovsky, *J. Vac. Sci. Technol. A-Vac. Surf. Films* 1986, **4**, 689.
- 51 H. Namduri and S. Nasrazadani, *Corrosion Sci.* 2008, **50**, 2493.
- 52 K. Q. Peng, Y. Wu, H. Fang, X. Y. Zhong, Y. Xu and J. Zhu, *Angew. Chem.-Int. Edit.* 2005, **44**, 2737.
- 53 W. L. Wilson, P. F. Szajowski and L. E. Brus, *Science* 1993, **262**, 1242.
- 54 B. S. Zou, J. P. Wang, C. Liu, J. Z. Zhang and M. A. El-Sayad, *Physical Review B* 2000, **62**, 16595.
- 55 J. Yuan and D. Haneman, *J. Appl. Phys.* 1999, **86**, 2358.
- 56 A. P. Li, G. F. Bai, K. M. Chen, Z. C. Ma, W. H. Zong, Y. X. Zhang and G. G. Qin, *Thin Solid Films* 1998, **325**, 137.
- 57 L. Skuja, *J. Non-Cryst. Solids* 1994, **179**, 51.
- 58 S. M. Prokes, *Appl. Phys. Lett.* 1993, **62**, 3244.
- 59 G. G. Qin, Y. M. Huang, J. Lin, L. Z. Zhang, B. Q. Zong and B. R. Zhang, *Solid State Commun.* 1995, **94**, 607.
- 60 G. Qin and G. G. Qin, *J. Appl. Phys.* 1997, **82**, 2572.

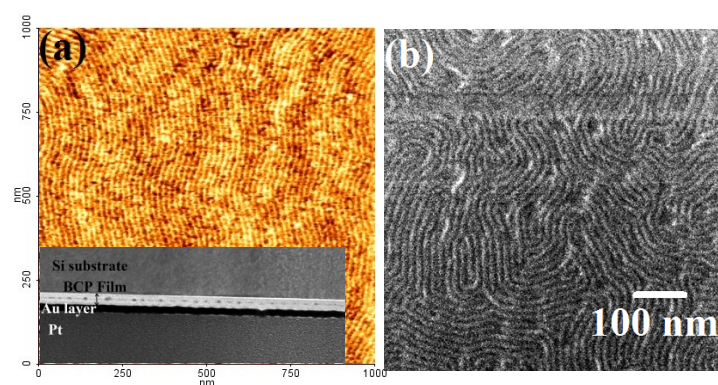
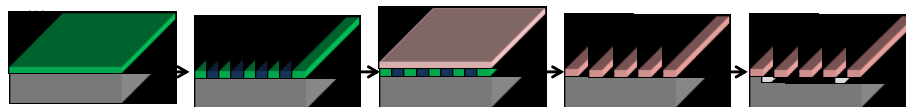


**Fig. 1** (a) Tapping mode AFM, (inset of a) Cross-sectional TEM and (b) SEM image of the surface morphology of the PS-*b*-PEO thin film following solvent annealing in toluene at 60° C for 30 min with the addition of 0.05 ml of LiCl-THF.



**Scheme 1** Schematic illustration of the fabrication of horizontal ordered Si nanowires on substrate. (A) PS-PEO thin film after spin coating (B) Perpendicularly oriented PS and PEO lamellae on the substrate after solvent annealing (C) Metal precursor solution spin coated on the template (D) oxide nanowires formed after UV/ozone treatment (E) Si nanowires fabricated by silicon ICP etch process.

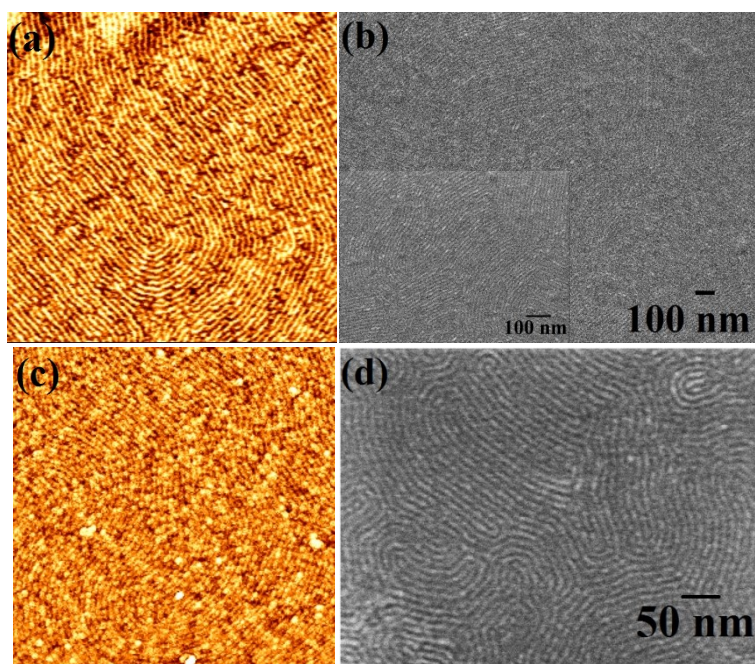


**Fig. 2** (a, c) AFM and (b, d) SEM images of iron oxide and nickel oxide nanowire arrays formed after UV/Ozone treatment respectively.

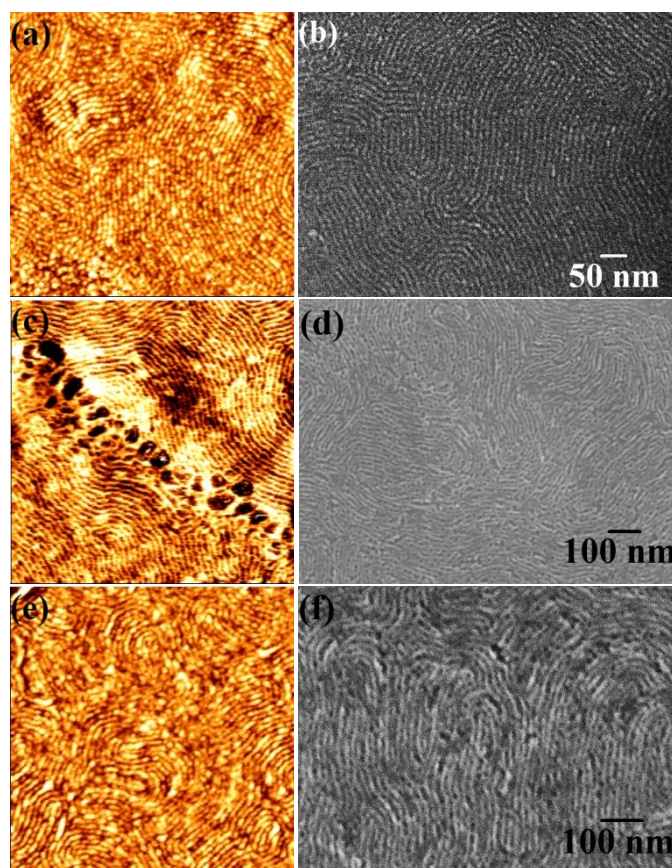


**Fig. 3** Surface morphology and topography of the iron oxide nanowires prepared with different concentrations of iron nitrate-2 propanol solution stirred for 30 min (a, b) 1.5 wt% (c, d) 2 wt% and (e, f) 2.2 wt% respectively.



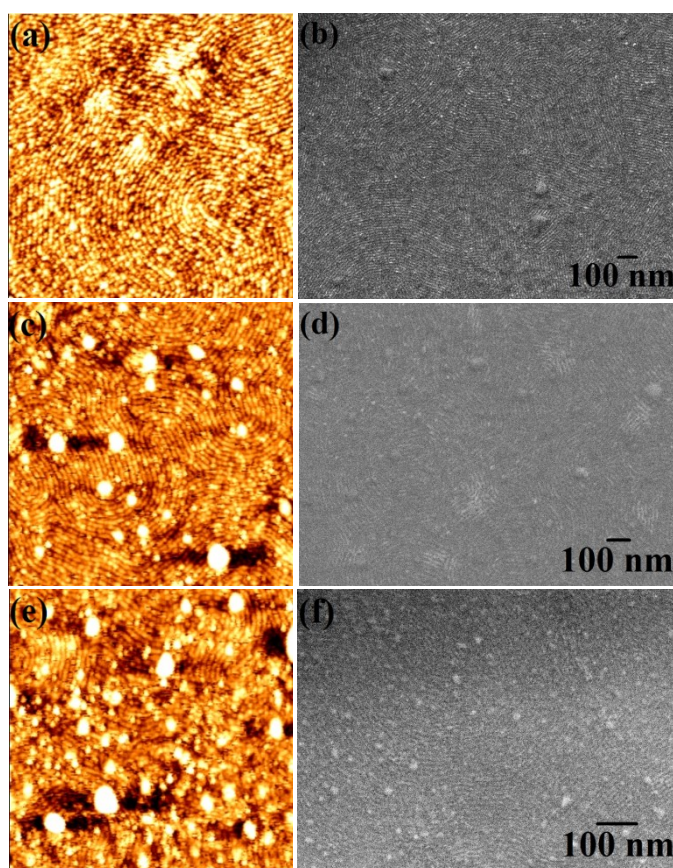


**Fig. 4** Surface morphology and topography of the iron oxide nanopatterns prepared with 1.8 wt% of iron nitrate-2 propanol solution stirred for different time of (a, b) 45 min (c, d) 1 h and (e, f) 1 h 30 min respectively.

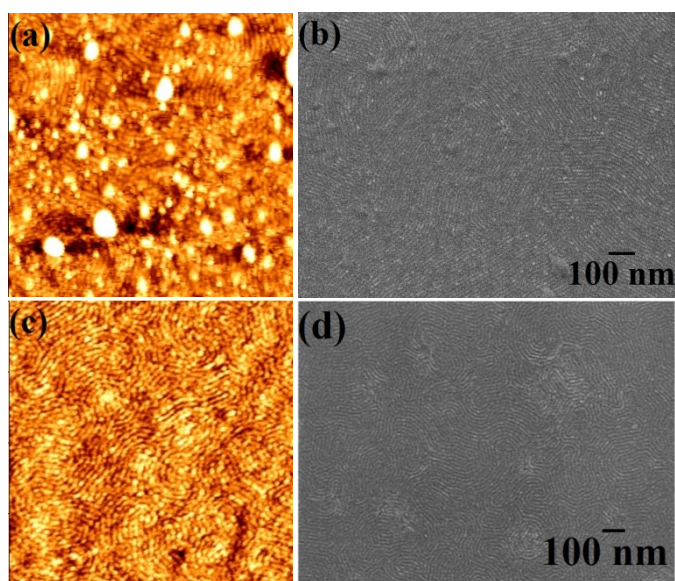


**Fig. 5** (a) AFM and (b) SEM images of iron oxide nanopatterns prepared with 1.8 wt% precursor dissolved in anhydrous ethanol stirred for 30 min. (c) AFM and (d) SEM images of iron oxide nanopatterns prepared with 1.8 wt% precursor dissolved in 2-propanol stirred for 30 min using LiCl-ethanol mediated BCP thin film.

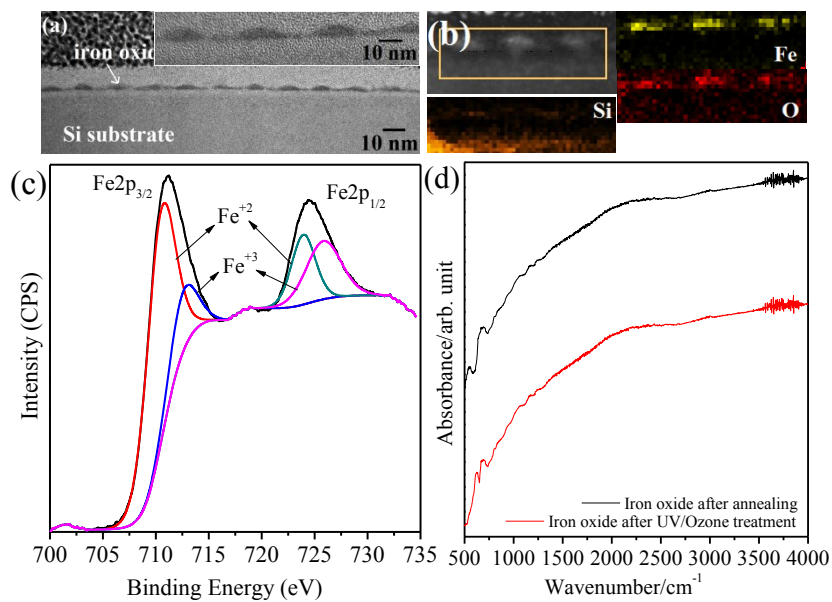


**Fig. 6** (a) Cross sectional TEM images of lamellar phase iron oxide nanowire arrays. (b) elemental mapping of Fe, O and Si. (c) Fe 2p spectra of iron oxide nanowires after UV/Ozone treatment (d) FTIR spectra of iron oxide nanowires after UV/Ozone treatment and further annealing.



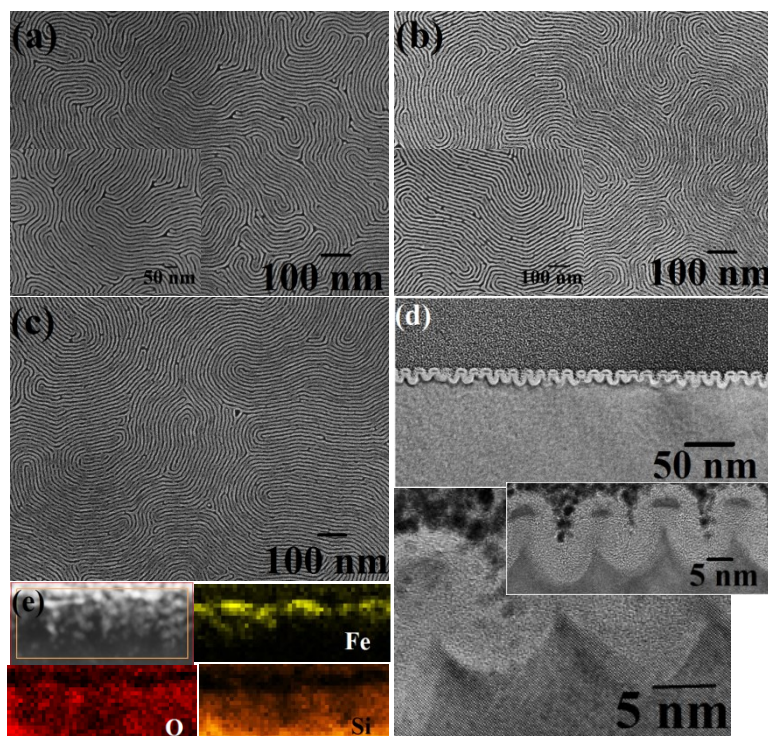


**Fig. 7** SEM images of Si nanowire arrays with iron oxide as a hard mask after (a) 30 sec (b) 45 sec and (c) 1 min Si etch respectively. (d) Cross sectional TEM and HRTEM images of Si nanowires with iron oxide at top. (e) elemental mapping of Fe, O and Si.

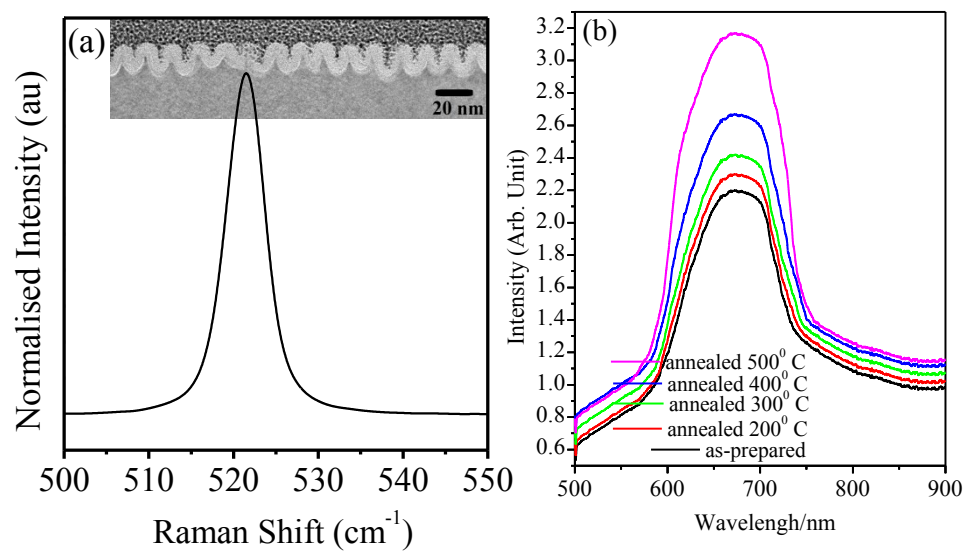


**Fig. 8** (a) Raman spectrum of Si nanowire arrays. (b) PL spectra of as-prepared Si nanowire arrays and annealed nanowires at different temperatures.